Journal of Materials Chemistry C

PAPER

View Article Online
View Journal | View Issue

Cite this: J. Mater. Chem. C, 2015, 3, 10554

Computational and experimental investigation of $TmAgTe_2$ and XYZ_2 compounds, a new group of thermoelectric materials identified by first-principles high-throughput screening†

Hong Zhu,‡[a] Geoffroy Hautier,[b] Umut Aydemir,[c] Zachary M. Gibbs,[d] Guodong Li,[c] Saurabh Bajaj,[c] Jan-Hendrik Pöhls,[e] Danny Broberg,[f] Wei Chen,[g] Anubhav Jain,[f] Mary Anne White,[d] Mark Asta,[e] G. Jeffrey Snyder,[c] Kristin Persson[f] and Gerbrand Ceder*[afg]

Received 20th May 2015,
Accepted 3rd August 2015

DOI: 10.1039/c5tc01440a

www.rsc.org/MaterialsC

A new group of thermoelectric materials, trigonal and tetragonal XYZ_2 (X, Y: rare earth or transition metals, Z: group VI elements), the prototype of which is $TmAgTe_2$, is identified by means of high-throughput computational screening and experiment. Based on density functional theory calculations, this group of materials is predicted to attain high zT (*i.e.* ~1.8 for p-type trigonal $TmAgTe_2$ at 600 K). Among approximately 500 chemical variants of XYZ_2 explored, many candidates with good stability and favorable electronic band structures (with high band degeneracy leading to high power factor) are presented. Trigonal $TmAgTe_2$ has been synthesized and exhibits an extremely low measured thermal conductivity of 0.2–0.3 W m^{-1} K^{-1} for $T > 600$ K. The zT value achieved thus far for p-type trigonal $TmAgTe_2$ is approximately 0.35, and is limited by a low hole concentration (~10^{17} cm^{-3} at room temperature). Defect calculations indicate that Tm_{Ag} antisite defects are very likely to form and act as hole killers. Further defect engineering to reduce such X_Y antisites is deemed important to optimize the zT value of the p-type $TmAgTe_2$.

1. Introduction

Thermoelectric materials are important for both waste heat harvesting and Peltier cooling, but their widespread application is limited by relatively low efficiency. Future applications of thermoelectrics will require the optimization of existing state-of-the-art materials (Bi_2Te_3, PbTe, $CoSb_3$, half Heuslers and others)[1–5] and the discovery of new materials with high figure of merit ($zT = S^2\sigma T/\kappa$ where S is the Seebeck coefficient, σ is the electrical conductivity, κ is the thermal conductivity, and T is the absolute temperature). The two broad strategies for improving zT are to enhance the power factor ($S^2\sigma$) and to reduce the thermal conductivity, κ, of the materials.

With the exponential growth in computing power and theoretical advances, materials search and discovery based on *ab initio* computational materials design are now feasible.[6,7] While this approach has been used to design high-strength steel,[8] high voltage and high rate lithium-ion batteries,[9] and catalysts,[10,11] limited attempts have been made to search for interesting thermoelectric materials (*i.e.*, with a focus on half Heuslers, transition metal silicides, or antimonide compounds).[4,12–16] The Materials Project (www.materialsproject.org) strives to be a community resource for density functional theory (DFT) electronic band structures, phase diagram prediction, and other applications.[17,18] Beginning last year, we initiated a high-throughput search for new thermoelectric materials within the Materials Project electronic structure database. To date, ~9000 potential thermoelectric candidates have been screened. Additional calculations are underway, and we plan to later publish a more thorough analysis of the high-throughput aspects of this project.

[a] Department of Materials Science and Engineering, Massachusetts Institute of Technology, 77 Massachusetts Avenue, Cambridge, Massachusetts, 02139, USA. E-mail: gceder@mit.edu
[b] Institute of Condensed Matter and Nanosciences (IMCN), Université catholique de Louvain, Chemin des étoiles 8, bte L7.03.01, Louvain-la-Neuve 1348, Belgium
[c] Materials Science, California Institute of Technology, 1200 E California Blvd, Pasadena, California, 99125, USA
[d] Division of Chemistry and Chemical Engineering, California Institute of Technology, 1200 E California Blvd, Pasadena, California, 99125, USA
[e] Department of Physics and Atmospheric Science, Dalhousie University, 6310 Coburg Rd, PO BOX 15000, Halifax, Nova Scotia B3H 4R2, Canada
[f] Department of Materials Science and Engineering, University of California, Berkeley Berkeley, California 94720, USA
[g] Lawrence Berkeley National Lab, 1 Cyclotron Rd., Berkeley, California 94720, USA

† Electronic supplementary information (ESI) available: Details of calculated electronic structure, defect and transport results. Details of PXRD, DSC, heat capacity and XPS. See DOI: 10.1039/c5tc01440a

‡ Current address: University of Michigan – Shanghai Jiao Tong University Joint Institute, Shanghai Jiao Tong University, Shanghai 200240, China.

In this manuscript, we report on a new group of thermoelectric materials identified from our high-throughput computational screening and experiment, namely, some octahedrally coordinated XYZ_2 materials (X stands for elements with a valence state of +3, Y = Ag, Cu, Au and Z = S, Se, Te), the prototypes of which are trigonal and tetragonal $TmAgTe_2$. Potentially high zT values are expected for this group of materials (*i.e.* $\sim$1.8 for p-type trigonal $TmAgTe_2$ at 600 K). Based on a data-mining chemical substitution algorithm,[19] we explored 500 chemical variants of XYZ_2 and found a large number of candidates with good stability and favorable electronic band structures (with high band degeneracy leading to high power factor). Among underlying correlations between chemistry and band convergence, we find that small X-d and Z-p hybridization in the trigonal phase and small Y-d and Z-p hybridization in the tetragonal phase favor a high band degeneracy, and hence a high zT value. Of the several promising compounds, we have synthesized trigonal $TmAgTe_2$, which exhibits an extremely low thermal conductivity of 0.2–0.3 W m^{-1} K^{-1} for $T > 600$ K (close to the glassy limit). Due to the limited hole concentration that could be attained so far ($\sim 10^{17}$ cm^{-3} at room temperature), the zT value achieved for the trigonal $TmAgTe_2$ sample is $\sim$0.35. First-principles defect calculations indicate that such a low hole concentration is likely correlated to the presence of Tm_{Ag} antisite defects, which donate electrons and reduce the attainable hole concentration. Proper defect engineering might be necessary to reduce the formation of X_Y antisite defects within the trigonal $TmAgTe_2$ and similar XYZ_2 compounds. Our work also points at the importance of evaluating the ability to dope materials when screening thermoelectric materials.

2. Results

2.1 Background and comparison to common thermoelectric materials

So far, we have studied $\sim$9,000 compounds in the International Crystal Structure Database (ICSD),[20,21] which have density functional theory computed band gaps larger than 0.5 eV. Recently, we initiated studies on the compounds in ICSD with smaller computed band gaps for thermoelectric applications, which require denser k-point meshes to better describe the band dispersion and transport properties. Among the materials screened so far, we identified those with the highest theoretical power factors, and further studied their stability based on the computed decomposition energy and estimated thermal conductivity (for selected compounds), to evaluate their potential as thermoelectric materials (see Computational and experimental methodologies section). Another factor in selecting compounds from the list was finding a good match with our synthesis capabilities and expertise.

Table 1 lists some representative candidates among different crystal structure classes. Table 1 includes some thermoelectric materials that are already well known and have been extensively studied, such as PbTe, PbSe, Si, TiCoSb and $InCuTe_2$—validating the method. Table 1 also includes materials known to exhibit high power factor (thereby also validating our power factor screening), but known to have too high thermal conductivity to yield favorable zT, such as AlSb and $SrTiO_3$.[5,22] A detailed discussion about these high throughput results, their assumptions, and validation will be the subject of a future publication.

Table 1 Several candidates with high power factors (PF) (within a constant relaxation time set to 10^{-14} s) at 600 K identified from our high throughput computational screening

	Space group	Predicted max p/n type PF (mW m^{-1} K^{-2})	Experimental reference
PbTe	$Fm\bar{3}m$	32.9/25.1	2, 45 and 84
PbSe	$Fm\bar{3}m$	14.7/4.1	52 and 85
$CoSb_3$	$Im3$	4.29/5.5	86 and 87
Si	$Fd\bar{3}m$	4.83/6.34	88 and 89
TiCoSb	$F\bar{4}3m$	14.7/7.2	90
$CuInTe_2$	$I\bar{4}2d$	4.3/3.2	24
AlSb	$F\bar{4}3m$	4.85/9.36	91–93
$SrTiO_3$	$Pm\bar{3}m$	7.29/6.95	94 and 95
$TmAgTe_2$	$P\bar{3}m1$	6.7/6.83	—
$TmAgTe_2$	$P\bar{4}2_1m$	4.99/3.64	—
$YAgTe_2$	$P\bar{4}2_1m$	5.05/3.94	—

We also found interesting materials that have not been considered as thermoelectrics, such as trigonal $TmAgTe_2$ ($P\bar{3}m1$) and tetragonal $TmAgTe_2$, $YAgTe_2$ ($P\bar{4}2_1m$) (see Table 1). The structure, thermal and electronic properties of trigonal and tetragonal $TmAgTe_2$ as well as an extensive substitutional study of $\sim$500 variants, namely trigonal and tetragonal XYZ_2 (X stands for elements with a valence state of +3, Y = Ag, Cu, Au and Z = S, Se, Te), are discussed in detail below.

2.2 Crystal structure of trigonal and tetragonal $TmAgTe_2$

In the trigonal $TmAgTe_2$ identified from our high throughput computations, the Tm atoms occupy half of the octahedral interstices and the Ag atoms occupy the other half, $Tm^{oh}Ag^{oh}Te_2$ (oh: octahedral hole, see Fig. 1(a)). As there is one $TmTe_2$ layer in the unit cell, trigonal $Tm^{oh}Ag^{oh}Te_2$ can be referred to as an O1 structure, according to the notation of Delmas *et al.* for layered chalcogenides.[23] This is different from the O3 type $NaCoO_2$, which has three CoO_2 layers in the unit cell. The computed lattice parameters for trigonal $Tm^{oh}Ag^{oh}Te_2$ are 4.342 and 6.998 Å for a and c, respectively, very close to our experimental measurements of 4.295(2) and 7.007(3) Å (see Section 2.7). Trigonal $Tm^{oh}Ag^{oh}Te_2$ is different from the $I\bar{4}2d$ chalcopyrite in the zinc-blende structure in which all cations are tetrahedrally coordinated, *i.e.* $Cu^{th}In^{th}Te_2$,[24] and the recently reported trigonal $TmCuTe_2$ with Tm in the octahedral site and Cu in the tetrahedral site ($Tm^{oh}Cu^{th}Te_2$, th: tetrahedral hole).[25]

Apart from the trigonal phase, one other polymorph (the tetragonal phase in the $P\bar{4}2_1m$ space group of $TmAgTe_2$) has been reported.[26] The tetragonal $TmAgTe_2$ has lower symmetry and larger volume (see Fig. S1 in ESI†), in which Ag and Tm intermix within the basal planes. Furthermore, Ag atoms shift from the octahedral sites (in the trigonal structure) to the tetrahedral sites (in the tetragonal structure) and we therefore represent the tetragonal phase as $Tm^{oh}Ag^{th}Te_2$. As shown in Fig. 1, the tetragonal $Tm^{oh}Ag^{th}Te_2$ is composed of a mixture of distorted $TmTe_6$ octahedra and $AgTe_4$ tetrahedra,[27,28] compared

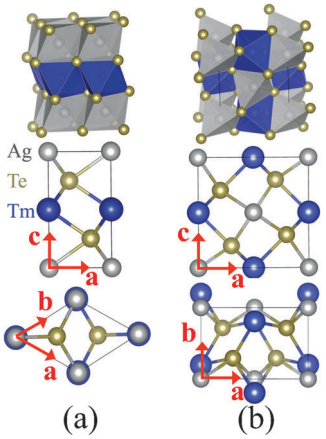

Fig. 1 The structure of $TmAgTe_2$ in the (a) $P\bar{3}m1$ trigonal and (b) $P\bar{4}2_1m$ tetragonal crystal structure. The top and bottom figures are the projections along the *b* and *c* directions, respectively. The blue, white, and yellow spheres represent Tm, Ag and Te atoms, respectively.

with the pure octahedra of $TmTe_6$ and $AgTe_6$ found in the trigonal phase. Our experimental lattice parameters of the tetragonal phase are found to be $a = c = 7.0831(5)$ Å and $b = 4.5298(7)$ Å, where the theoretical values are 7.0655 Å and 4.6903 Å, respectively.

The tetragonal (trigonal) phase is considered to be the low (high) temperature phase.[27–29] This is consistent with our 0 K calculations in which the tetragonal $Tm^{oh}Ag^{th}Te_2$ is ~15 meV per atom lower in energy than the trigonal phase. Recent experimental work, in which the $XAgTe_2$ samples were annealed at 870 K and quenched in air, suggest that X = Tm prefers the formation of the trigonal phase whereas compounds with X = Y, Tb, Dy, Ho and Er preferentially form the tetragonal phase.[27,28]

2.3 Thermal conductivity of $TmAgTe_2$

Unlike tetragonal chalcopyrite with pure tetrahedrally coordinated cations, at least one cation in trigonal $Tm^{oh}Ag^{oh}Te_2$ and tetragonal $Tm^{oh}Ag^{th}Te_2$ exhibit octahedral coordination (see Fig. 1), which is expected to lead to lower lattice thermal conductivity, κ_{lat}, as higher coordination has been correlated with low thermal conductivity.[30] Following the Cahill–Watson–Pohl model[31] (see Computational and experimental methodologies section), we calculated the average κ_{lat} in the amorphous limit (κ_{min}) to be 0.36 and 0.37 W m^{-1} K^{-1} for trigonal and tetragonal $TmAgTe_2$, respectively.

Using the Vaschenko–Zubarev formulation ($\gamma = K'/2 - 5/6$, in which K' is the pressure derivative of the bulk modulus, K)[32] and fitting the total energy of the relaxed structure at different volumes to the Murnaghan equation of state ($E(V) = E(V_0) + \frac{KV}{K'}\left[\frac{(V_0/V)^{K'}}{K'-1} + 1\right] - \frac{KV_0}{K'-1}$, in which V_0 is the equilibrium volume),[33] we determine that the trigonal $Tm^{oh}Ag^{oh}Te_2$ has high anharmonicity with a Grüneisen parameter (γ) computed to be 1.37. A large γ is usually favorable as it leads to lower thermal conductivities,[34] although we emphasize that this parameter represents only an indicator amongst several factors determining the thermal conductivity. We note that by comparison,

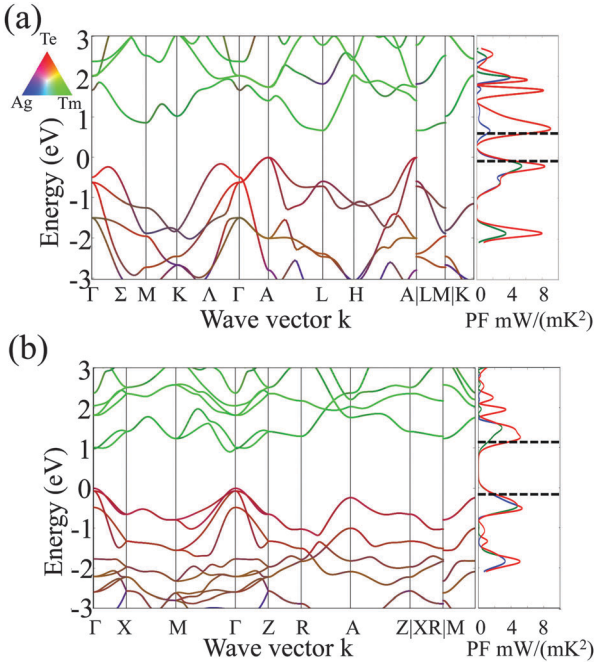

Fig. 2 The computed band structure and power factor at 600 K of (a) trigonal $Tm^{oh}Ag^{oh}Te_2$ and (b) tetragonal $Tm^{oh}Ag^{th}Te_2$. The color in the band structures represents the projections of the wave function onto different elements, where red, blue and green are associated with Te, Ag and Tm, respectively. In the right panels, the power factors along the three crystallographic directions *a*, *b*, and *c* are indicated by different colors. The maximum power factor occurs at carrier concentration of 4.8×10^{20} (3.5×10^{21}) and 5.8×10^{20} (3.8×10^{20}) cm^{-3} for holes and electrons in trigonal (tetragonal) $TmAgTe_2$, respectively. The horizontal dashed lines stand for the Fermi level at which the carrier concentration is 10^{20} cm^{-3}. The transport values have been obtained in the constant scattering time approximation (10^{-14} s).

PbTe (known to exhibit low thermal conductivity) is predicted to have a similar Grüneisen parameter (computed value of 1.4 compared to the experimental value of 1.45).[35]

Considering that low thermal conductivities, close to the amorphous limit, have been reported for some silver chalcogenides (*i.e.*, Ag_2Te, AgCrSe, $AgSbTe_2$)[25,36,37] and copper chalcogenides (*i.e.*, $CuGaTe_2$, Cu_2Se, Cu_2S, $CuInTe_2$, $BaCu_{5.9}SeTe_6$),[24,38–41] a low thermal conductivity is expected for $TmAgTe_2$ and related compounds, as validated from our experiments discussed in Section 2.7.

2.4 The electronic structure and transport property of $TmAgTe_2$

As shown in Fig. 2, both the trigonal and tetragonal phases display band structures interesting for thermoelectrics—having multiple bands close to the valence band maximum (VBM) and the conduction band minimum (CBM). We note that these band structures are calculated with no spin–orbit coupling (NSOC); SOC corrections are discussed later in this section. In the NSOC band structure, the valence band of trigonal $Tm^{oh}Ag^{oh}Te_2$ contains pockets at the A point and along Σ and Λ directions that are close in energy, and which have multiplicity of 1, 6 and 6 in the full Brillouin zone, respectively. The p-type tetragonal

phase has 4 pockets at Γ and 2 pockets at A. As can be seen from Fig. 2, such a high band degeneracy correlates with the high computed power factor and hence is favorable for thermoelectrics. The optimum power factor is thought to scale with the quality factor, $B = \frac{2k_B{}^2\hbar}{3\pi}\frac{N_v C_l}{m_I{}^* E_{def}{}^2 \kappa_{lat}}$, in which N_v is the number of degenerate Fermi surfaces, $C_l = v_l{}^2 d$ (where v_l is the longitudinal speed of sound and d is density), $m_I{}^*$ is the inertial (or conductivity) effective mass, and E_{def} is the electronic deformation potential.[42,43] The predictive power of B based on semi-empirical approaches rooted in DFT calculations has been recently demonstrated for a range of known thermoelectric materials.[44] Based on this equation, systems containing many degenerate pockets should yield good thermoelectrics, as is the case here for $TmAgTe_2$ (each band maintains its curvature or carrier mobility while increasing the overall Seebeck coefficient[17,45]).

Although both p- and n-type materials are interesting from a theoretical standpoint, we will focus our discussion on the p-type results because their power factor is more isotropic and our experimental and theoretical results indicate that trigonal $Tm^{oh}Ag^{oh}Te_2$ is intrinsically p-type. The two polymorphs show high computed power factor (under a constant relaxation time approximation) with the three eigenvalues of the power factor tensor for the trigonal phase close to 5, 5, and 8 mW m^{-1} K^{-2} and the three eigenvalues for the tetragonal phase close to 5 mW m^{-1} K^{-2}.

Considering that the top of the valence band is dominated by states with character corresponding to the chalcogenide atoms, we have compared the NSOC and SOC band structures for p-type $TmAgTe_2$ (see Fig. S2 and S3 in the ESI†). For trigonal $Tm^{oh}Ag^{oh}Te_2$ with the inclusion of SOC, the doubly degenerate valence bands at the A point in the NSOC band structure split by $\sim$0.5 eV. This increases the energy difference between the valence band maxima at the A point and along the Λ direction by $\sim$0.15 eV compared to the NSOC band structure.

The SOC effect is smaller in tetragonal $Tm^{oh}Ag^{th}Te_2$: it increases the band separation at Γ point by only $\sim$0.1 eV compared to the NSOC case. For trigonal selenide (*i.e.*, $PrAgSe_2$ in Fig. S4, ESI†), the band splitting at the A point due to SOC is 0.2 eV, which increases the energy separation between the A band and the Λ valence bands by 0.06 eV. SOC is found to have a negligible effect on the electronic structure for sulfide materials (see the example of $YAgS_2$ in Fig. S5, ESI†).

Thus, a lower band degeneracy might be expected due to the effect of spin orbit coupling, especially for tellurides. In the worst case (trigonal $Tm^{oh}Ag^{oh}Te_2$), the average maximum power factor predicted from the SOC calculation over the three trigonal crystallographic directions a, b, and c is $\sim$4.2 mW m^{-1} K^{-2} at 600 K (still a high value), compared with $\sim$6.7 mW m^{-1} K^{-2} determined from an NSOC calculation.

2.5 Defect chemistry in trigonal $Tm^{oh}Ag^{oh}Te_2$

Fig. 3 plots the Tm–Ag–Te ternary ground state phase diagram from the Materials Project database,[46,47] and Fig. 4 shows the calculated defect formation enthalpies as a function of Fermi level μ_e for the trigonal $TmAgTe_2$ compound. The phase diagram and defect calculations for the tetragonal phase (*i.e.* $Y^{oh}Ag^{th}Te_2$) are provided in Fig. S6 and S7 in the ESI† with the same relative order of defect stability compared to trigonal $Tm^{oh}Ag^{oh}Te_2$. For all growth conditions (area 1–4 in Fig. 4 and Fig. S7, ESI†), the lowest energy defects for such XYZ_2 compounds are either the cation antisite defects (X_Y) or the cation vacancy defects (V_X or V_Y). In areas 1 and 3, which are X-poor and Y-rich, the hole donating V_X or V_Y defects dominate the material, making it p-type. Under a charge neutrality condition where the sum of the intrinsic hole concentration, intrinsic electron concentration and the intrinsic defect's charge density equals to zero,[48] we have determined the equilibrium carrier concentration at 300 K for trigonal $Tm^{oh}Ag^{oh}Te_2$ in Table S1 (ESI†). We note that a hole concentration in the order of 10^{20} cm^{-3} could be achievable for Tm poor and Ag rich conditions, *i.e.*, in areas 1 and 3. In area 2, the defect charges of the X_Y cation antisite and V_Y vacancy defect compensate each other leading to a low hole carrier concentration compared to areas 1 and 3. Finally, in area 4, which is X-rich and Y-rich, the antisite X_Y defect is predicted to lead to an n-type material. Thus, to obtain the optimum thermoelectric properties, the p-type intrinsic XYZ_2 compounds should be synthesized along the direction of stability of the Y_2Z phase in X-poor, Y-rich, and Z-poor conditions, *i.e.*, Ag_2Te for trigonal $Tm^{oh}Ag^{oh}Te_2$ in areas 1 and 3 of Fig. 4.

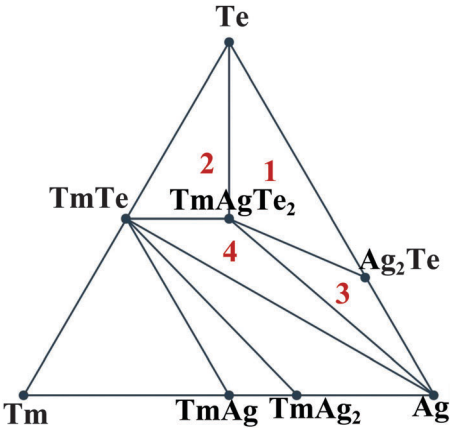

Fig. 3 Ground state phase diagrams of the Tm–Ag–Te system from the Materials Project Database. Different synthesis regions of the XYZ_2 compounds, as defined by the different three-phase equilibria that $TmAgTe_2$ can be part off, are denoted by the numbers.

2.6 Substitution results

Both trigonal and tetragonal phases of $TmAgTe_2$ are predicted to be promising thermoelectric materials because band structures favor high power factor and low thermal conductivity. It is thus of interest to explore other possible chemistries in these two crystal structures. We conducted a systematic high-throughput substitutional search by computing stability and power factor for approximately 500 XYZ_2 compounds in the trigonal and tetragonal phases. These compounds were generated by a substitution algorithm that employs data-mined statistics from all known crystalline compounds,[19] and captures how easily elements substitute for each other.[49]

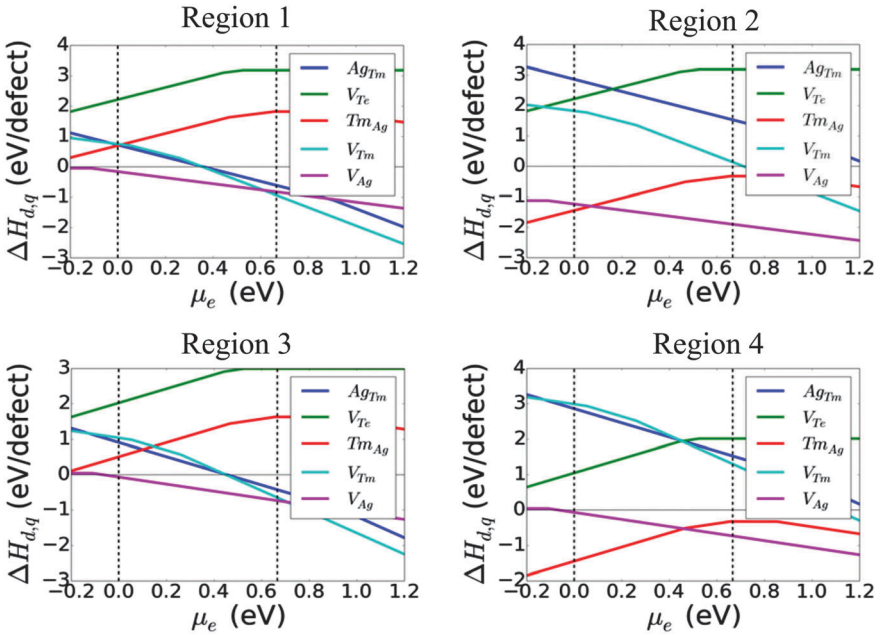

Fig. 4 Calculated defect formation enthalpies $\Delta H_{d,q}$ in trigonal $Tm^{oh}Ag^{oh}Te_2$ as a function of Fermi level, μ_e, plotted for chemical potentials corresponding to four different 3-phase regions as labeled in Fig. 3. Vertical dashed lines represent the calculated band edges.

By assuming κ_{lat} of 0.5 W m^{-1} K^{-1} for all compounds, we estimated the zT value at 600 K. The assumed κ_{lat} = 0.5 W m^{-1} K^{-1} is similar to the experimental κ for trigonal $TmAgTe_2$ at 600 K, ~0.3 W m^{-1} K^{-1} (see Section 2.7). Fig. 5 plots the maximum average zT over three crystallographic directions at 600 K for holes (or p-type) *versus* decomposition energy (E_{decomp}) of XYZ_2. For candidate compounds with $zT > 1.5$, the chemical formula is shown. Similar plots of average zT value for electrons *versus* E_{decomp} are provided in Fig. S8 of ESI.†

As we can see from Fig. 5, E_{decomp} of XYZ_2 with Z = Te is usually lower than that of sulfide compounds. For example, E_{decomp} of trigonal $TmAgZ_2$ increases with Z changing from Te to Se and S. This can be understood by the increasing size of the octahedron formed by the six chalcogenide atoms in the trigonal structure as one moves to larger chalcogenides. An increasing octahedron favors X or Y atom at the octahedral sites (detailed histograms of the E_{decomp} for trigonal XYZ_2 can be found in Fig. S9 in the ESI†). We also note from Fig. 5 that there are many trigonal $X^{oh}Ag^{oh}Z_2$ compounds and tetragonal $X^{oh}Cu^{th}Z_2$ compounds present within the low E_{decomp} window. Since the atomic radius of Ag (1.6 Å) is larger than for Cu and Au (1.35 and 1.35 Å),[50] the atomic size of the Y atom (R_Y) also affects the relative stability of the trigonal and tetrahedral structures—a large (or small) Y atom in XYZ_2 is more likely to sit at a large-space octahedral (or small-space tetrahedral) site, preferring the formation of a trigonal (or tetragonal) phase, respectively.

Besides trigonal $Tm^{oh}Ag^{oh}Te_2$ with predicted maximum zT ~ 1.8, we found many candidates for thermoelectrics in both trigonal and tetragonal crystal structures having zT larger than 1.5, such as trigonal $ScAgSe_2$, $TmCuTe_2$, $YAgTe_2$, $LuAgSe_2$, and tetragonal $ScCuSe_2$, $PrAgTe_2$ *etc.* From a careful inspection of the band structure of these high zT materials it is found that these materials all have multiple band extrema at the band edges. In Fig. 6, we show the correlation between maximum zT and energy difference between the two highest valence band maxima found in the trigonal XYZ_2 compounds, namely the A band and the Λ band. Here only compounds with decomposition energy smaller than 0.05 eV per atom are shown. The results demonstrate how zT increases with a decreased energy separation of these two bands. It will therefore be of great interest to converge bands close to the band edges of these thermoelectric materials, *e.g.* through alloying or strain,[17,45,51,52] to enhance the band degeneracy (N_v) and hence the zT value for a given lattice thermal conductivity.

2.7 Preliminary experimental results on $TmAgTe_2$

$TmAgTe_2$ samples were synthesized by annealing in sealed quartz tubes (see Methods section for full details). The trigonal phase was obtained as almost single phase after quenching from 873 K to room temperature (Fig. 7). This phase slowly transformed to tetragonal at low temperatures, as indicated by the observation of a small fraction of the tetragonal phase in an XRD scan after annealing for 1 day at 673 K (Fig. S10, ESI†). A complete transformation to the tetragonal phase took place after further annealing for 3 days at 673 K (Fig. 7 and Fig. S10, ESI†). From differential scanning calorimetry (DSC) experiments, we observed that the tetragonal phase undergoes a phase transition to the trigonal phase at around 725–735 K (Fig. S11, ESI†). Once the trigonal phase forms, it does not transform quickly to the low-temperature tetragonal phase within the time scale of the transport measurements and shows metastable behavior at low temperatures (Fig. S12, ESI†). The composition of the tetragonal $TmAgTe_2$ sample was determined by EDXS as $Tm_{0.99}Ag_{1.02}Te_{1.99}$, very close to the nominal composition.

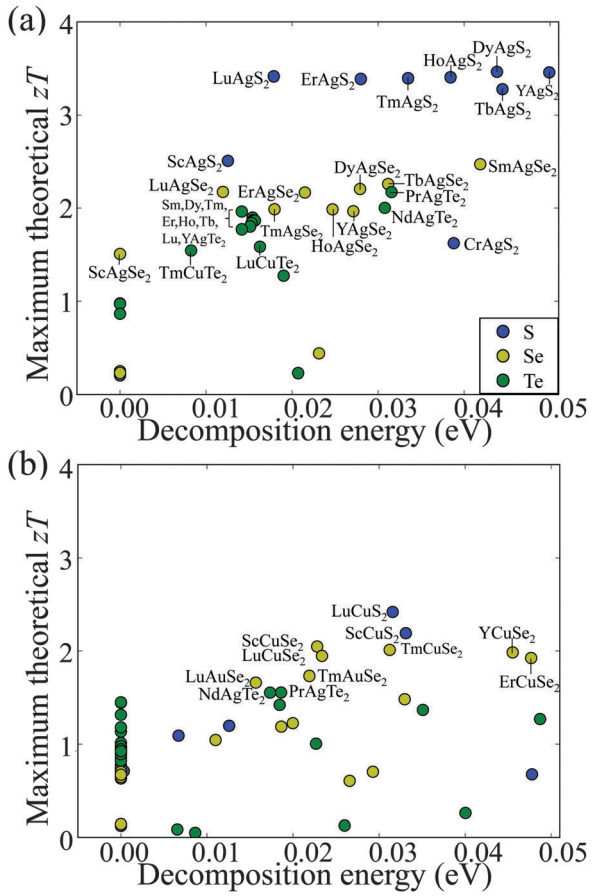

Fig. 5 Predicted maximum zT values at 600 K *versus* decomposition energy per atom for p-type XYZ_2 candidate compounds in (a) $P\bar{3}m1$ and (b) $P\bar{4}2_1m$ space groups. Sulfide, selenide and telluride are shown in blue, yellow and green, respectively. The compositions of the candidates with $zT > 1.5$ are indicated in the figure. For clarity, we only show a small window of E_{decomp} (<0.05 eV per atom). κ_{lat} is assumed to be 0.5 W m^{-1} K^{-1} for all the compounds.

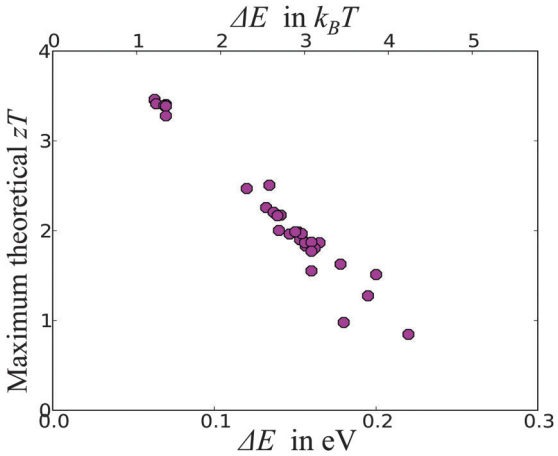

Fig. 6 Maximum p-type zT *versus* energy difference (ΔE) between the two highest valence band maxima (*i.e.*, at A point and along Λ direction) for trigonal $X^{oh}Y^{oh}Z_2$ compounds with non-zero band gap and small decomposition energy (<0.05 eV per atom) suggesting that zT should improve as the bands are closer to convergence.

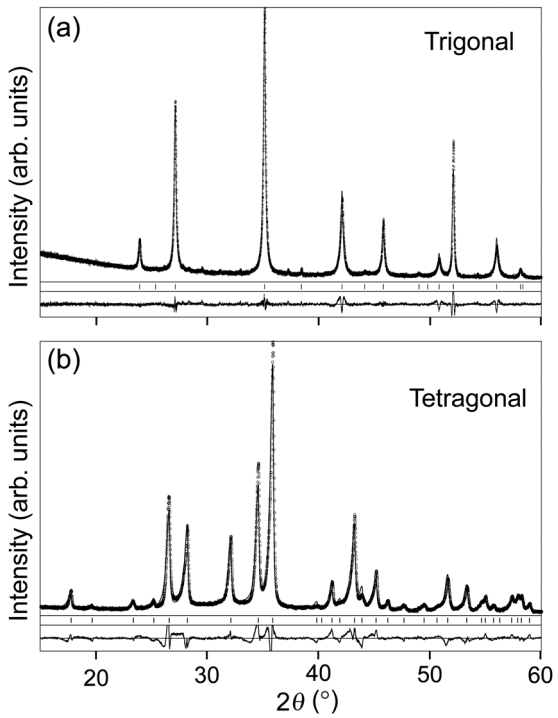

Fig. 7 XRD patterns of $TmAgTe_2$ (Cu-Kα radiation). The ticks mark the calculated reflection positions of trigonal $Tm^{oh}Ag^{oh}Te_2$ (space group: $P\bar{3}m1$) and tetragonal $Tm^{oh}Ag^{th}Te_2$ (space group: $P\bar{4}2_1m$) based on reported structure data[26,28] and the lowest lines correspond to the residuals of Rietveld refinements.

The electrical resistivity results for trigonal $TmAgTe_2$ display intrinsic semiconducting behavior up to 550 K with very low carrier concentration ($\sim 10^{17}$ cm^{-3} at room temperature) and a corresponding high Seebeck coefficient (Fig. 8). Optical absorption measurement of the trigonal phase indicates a band gap of around 0.54 eV (Fig. S13, ESI†), compared to the NSOC and SOC values of 0.69 and 0.4 eV, respectively. Above 550 K the carrier concentration decreases which leads to an increase in resistivity and Seebeck coefficient. With a similar carrier concentration, the tetragonal sample also showed semiconducting behavior above 450 K. Below 450 K, the resistivity increased with temperature. As mentioned previously, it is known that silver chalcogenide based compounds can achieve very low thermal conductivities.[36,53] For $TmAgTe_2$, a thermal conductivity close to the minimum calculated value and among the lowest attainable in any bulk thermoelectric material (as low as 0.25 W m^{-1} K^{-1} for the trigonal phase) was determined experimentally. The thermal conductivity was calculated from the thermal diffusivity using the experimental heat capacity shown in Fig. S14 (ESI†). The heat capacity of the trigonal phase is nearly constant above 450 K ($\sim$0.20 J g^{-1} K^{-1}), slightly above the Dulong–Petit value (0.19 J g^{-1} K^{-1}). Although the heat capacity data have a larger uncertainty than usual due to the extremely low thermal conductivity, resulting in low thermal coupling to the platform and low sample contribution to the total heat capacity, as per recommendations described in ref. 54, the uncertainty is less than 10%. Using the experimentally measured longitudinal

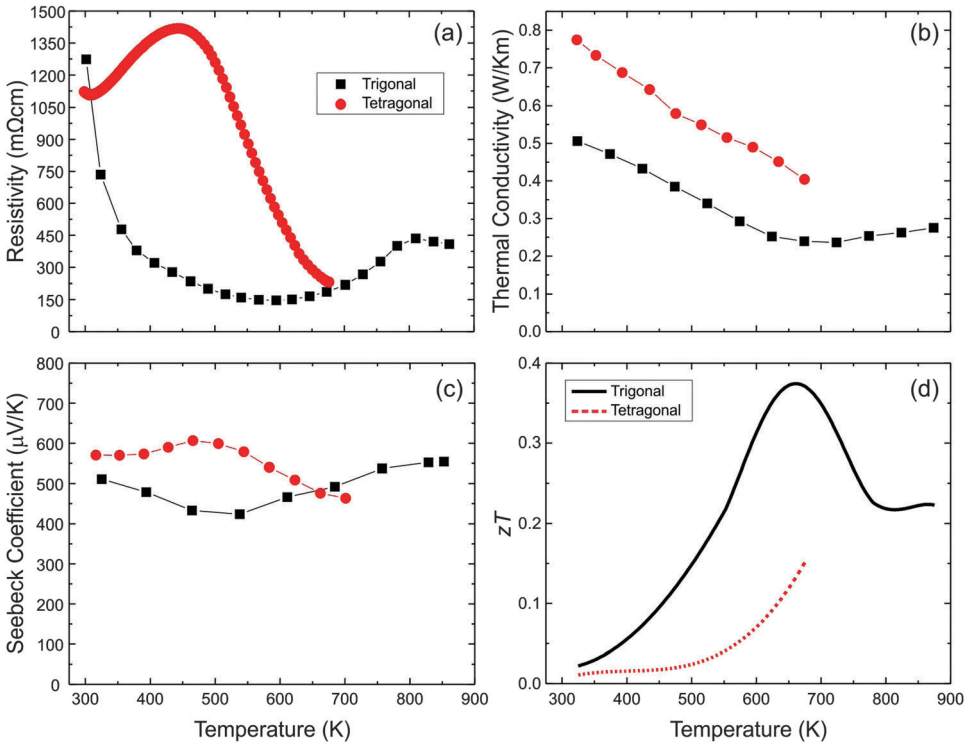

Fig. 8 The measured temperature dependence of (a) electrical resistivity, (b) thermal conductivity, (c) Seebeck coefficient and (d) zT of trigonal $Tm^{oh}Ag^{oh}Te_2$ (black) and tetragonal $Tm^{oh}Ag^{th}Te_2$ (red).

and transverse velocities of trigonal $Tm^{oh}Ag^{oh}Te_2$ ($v_{L,s}$ = 3520 and $v_{T,s}$ = 1390 m s^{-1}) and tetragonal $Tm^{oh}Ag^{th}Te_2$ ($v_{L,s}$ = 2810 and $v_{T,s}$ = 1625 m s^{-1}), we determined κ_{min} to be 0.38 and 0.36 W m^{-1} K^{-1}, comparable to the theoretical predications (0.36 and 0.37 W m^{-1} K^{-1}). This feature is very promising for thermoelectric materials and implies that if a reasonable power factor is obtained, thermoelectric materials with high zT values can be produced. Further doping studies are in progress to tune the carrier concentration in $TmAgTe_2$ related compounds in order to optimize the power factor.

3. Discussion

Using high-throughput computations, we have identified a series of XYZ_2 compounds with trigonal and tetragonal crystal structures that show promising properties for thermoelectric applications. Within a small E_{decomp} window, we uncovered a wide range of octahedrally coordinated, rare-earth silver chalcogenides in the trigonal phase and rare-earth copper chalcogenides in the tetragonal phase, both of which have favorable calculated zT values that can exceed 1.5 at 600 K for holes (as well as for electrons as shown in Fig. S8 in the ESI†).

We have also shown that the high zT value strongly correlates to the high band degeneracy found in these materials for a given κ_{lat}. It is thus of interest to understand which chemical or structural features lead to such a high band degeneracy. For both structures, the character of the electron states at the band edges is similar, with valence bands being mainly composed of Z-p, Y-d orbitals (see Fig. 2). If X contains d orbitals, it contributes to the p-d hybridization at the top of valence band and influences the relative positions of several valence band extrema. Chemistry is one simple approach to vary the hybridization. We found that reducing the orbital hybridization between X and Z atoms in the trigonal phase, or between Y and Z atoms in the tetragonal phase, leads to a higher band degeneracy at the valence band maxima. For example, as we can see from Fig. 9, the trigonal $Lu^{oh}Ag^{oh}Z_2$ and $Lu^{oh}Cu^{oh}Z_2$ with Z = S gives rise to the highest predicted zT, which is correlated to the large energy difference between Lu-d and S-p atomic orbitals and hence smaller X-d and Z-p orbital hybridization, compared to the case for Z = Se or Te. Unlike the trigonal phase, the top of the valence band for the tetragonal structure is more dominated by Y-d and Z-p orbitals because this hybridization is stronger in YZ_4 tetrahedron than in XZ_6 octahedron. For the tetragonal phase, the largest energy difference between Y-d and Z-p for $Lu^{oh}Ag^{th}Z_2$ and $Lu^{oh}Cu^{th}Z_2$ is found in $Lu^{oh}Ag^{th}Te_2$ and $Lu^{oh}Cu^{th}S_2$ (Fig. 9), and these compounds also exhibit high theoretical zT values.

Another approach to tune the band alignment is through the lattice parameter. For example, for the trigonal $Tm^{oh}Ag^{oh}Te_2$ at its equilibrium lattice parameter, the energy difference between the two highest valence bands (ΔE) is determined to be 0.17 eV from NSOC calculations. With a volume expansion (2% increase for each lattice direction), ΔE is reduced to 0.08 eV. Thermoelectric materials, especially those found in high temperature energy generators, usually undergo volume changes due to thermal expansion. If we assume that the thermal expansion

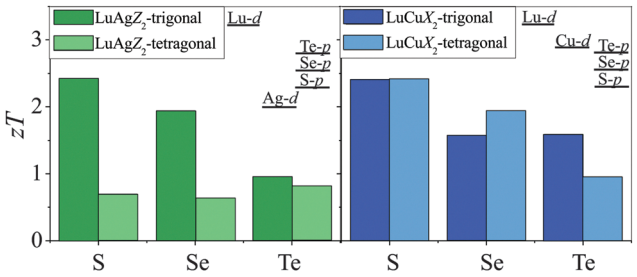

Fig. 9 The maximum theoretical zT of trigonal and tetragonal $LuAgZ_2$ and $LuCuZ_2$. The relative positions of computed atomic orbitals for Lu-d, Ag-d, Cu-d, Te-p, Se-p and S-p are schematically shown in the figure. κ_{lat} is assumed to be 0.5 W m^{-1} K^{-1} for all the compounds.

coefficient is similar to that of PbTe (2×10^{-5}),[55] ~2% lattice change could be attained at 900 K. This means that at high operating temperatures the band structures of these materials would have smaller band separation, *i.e.*, higher band degeneracy.[45,56]

Because we neglected SOC in our high-throughput calculations, we expect some overestimation of zT, especially for p-type trigonal tellurides. But considering its low computed and measured κ_{lat}, potential thermal-expansion-induced band convergence, effective band convergence at high temperature (bands within a few kT are effectively converged)[45] and reasonable power factor predicted from SOC calculations (*i.e.*, ~4 mW m^{-1} K^{-2} for trigonal p-type $TmAgTe_2$ at 600 K), trigonal tellurides are still interesting candidates for thermoelectric applications.

The κ_{min} of trigonal and tetragonal $TmAgTe_2$ are predicted from DFT calculations to be ~0.37 W m^{-1} K^{-1}. Our experimental measurements indicate trigonal $TmAgTe_2$ could have κ as low as 0.25 W m^{-1} K^{-1}. The predicted κ_{min} is slightly larger than the experimentally determined thermal conductivity. Similarly, low thermal conductivities have been reported for other silver or copper chalcogenides, *i.e.*, Ag_2Te/Se,[36,57] $AgCrSe_2$,[58] $AgSbTe_2$,[37] Cu_2Se,[39] for which κ_{lat} have been reported close to κ_{min} in the entire measured temperature range (300–650 K). This is thought to be related to the highly disordered structure and the high mobility with liquid-like diffusion coefficient of Ag or Cu atoms at high temperature.[36,39,59] Considering that the experimentally observed thermal conductivity of $TmAgTe_2$ at $T > 600$ K is smaller than the lattice thermal conductivity we used to compute zT, these XYZ_2 materials may give even higher zT values.

A measured zT value of ~0.35 is currently achieved at ~650 K for the p-type trigonal $Tm^{oh}Ag^{oh}Te_2$ sample; further improvement should be possible with a higher hole concentration in the order of 10^{19} cm^{-3} (as shown in Fig. S15 in ESI†). Our defect calculations indicate that the formation of X_Y antisites in XYZ_2 is likely to be responsible for the low measured hole concentration (10^{17} cm^{-3} in trigonal $Tm^{oh}Ag^{oh}Te_2$ at room temperature). On the other hand, the experimental findings on the larger c/a ratio for the layered trigonal $Tm^{oh}Ag^{oh}Te_2$ sample (1.63) compared to that of theoretical value of 1.61 indicate the presence of such Tm_{Ag} antisite defects in the sample, as the atomic radius of Tm (1.75) is larger than that of Ag (1.29) and the formation of Tm_{Ag} antisite defects will increase the c lattice parameter. Our defect calculations also indicate that such X_Y antisite defects could be suppressed by control of the preparation conditions (*i.e.* area 1 and 3 for trigonal $Tm^{oh}Ag^{oh}Te_2$). Defect engineering (*i.e.*, by decreasing the atomic size of Y atoms, $R_{Cu} < R_{Ag}$, we could reduce the void size for Y vacancy, V_Y) is an alternate way to control the formation of X_Y antisite defects (or the filling of an X atom to a Y vacancy void). The recently reported trigonal $Tm^{oh}Cu^{th}Te_2$ with tetrahedral-coordinated Cu atoms[25] has been reported to have a zT value of 0.81 at 745 K, due to its higher carrier concentration compared to that of the trigonal $Tm^{oh}Ag^{oh}Te_2$ with octahedral coordination of Ag atoms in this work. Sample optimization is currently in progress *via* a combined theoretical and experimental approach.

4. Conclusion

From our high throughput computations based on the Materials Project infrastructure, we have screened ~9000 materials and identified a new group of thermoelectric materials, trigonal and tetragonal $TmAgTe_2$, for which we generated ~500 variants (namely XYZ_2) using data-mining based substitution algorithms. This family of thermoelectric materials has low measured thermal conductivity (*i.e.*, 0.2–0.3 W m^{-1} K^{-1} for $T > 600$ K for trigonal $Tm^{oh}Ag^{oh}Te_2$). We also found a strong correlation between band degeneracy and maximum zT value, indicating the possibility for further optimization through band structure engineering (*i.e.*, through changes in lattice or chemistry). These new thermoelectric materials are likely to have advanced thermoelectric performance compared to the well-known zinc-blende-based copper chalcogenide thermoelectric materials, especially due to their high achievable band degeneracy and lower κ_{lat}. So far, the attainable zT value for trigonal $Tm^{oh}Ag^{oh}Te_2$ sample is ~0.35 due to the low hole concentration ~10^{17} cm^{-3}. Defect engineering to increase the carrier concentration and hence zT is currently in progress through a joint effort in which experimental optimization is guided through extensive theoretical defect calculations.

5. Computational and experimental methodologies

High-throughput computations and screening

All density functional theory (DFT) calculations in this work were performed using the Vienna Ab initio Simulation Package (VASP)[60] with the Perdew–Burke–Ernzerhof (PBE)[61,62] generalized gradient approximation (GGA) and the projector augmented-wave (PAW)[63] pseudopotentials. Although including an onsite Hubbard-type U term in DFT for f electrons enables a more accurate treatment of correlated electrons, difficulty to converge to the ground state has been observed due to the orbital physics inherent in the DFT+U scheme.[64,65] For example, using GGA+U for trigonal $TmAgTe_2$, the plus-U ramping methods suggested by Meredig *et al.*[64] as well as the orbital occupation scheme approach suggested by Allen *et al.*[66] for an f-12 orbital configuration, still resulted in several different self-consistent solutions with the same U value, the energy of which could vary by ~1 eV per formula. Of particular concern was the possibility

of f-electrons near the valence band or within the gap in some of the calculations. Therefore, we tested and ruled out this possibility by (i) switching from the DFT+U method to the hybrid HSE06 functional and (ii) verifying consistency between the HSE06 calculation and experimental XPS measurements (see X-ray photoelectron spectroscopy section). Moreover, using an empirical model that utilizes the behavior in the experimental energy difference between the localized $4f^n$-states, the 5d-derived conduction band and p-derived valence band, it has been reported that the occupied localized f states for trivalent lanthanide chalcogenides are usually lower than the valence band maxima with a character of chalcogenide-p orbital. For most of the rare earth elements, the unoccupied f states are higher than the conduction band minima (CBM) with a character of rare earth d orbital, but sit right around CBM for Tm_2Te_3.[67] In light of these difficulties, we use pseudopotentials in which the valences are set to 3 and the remaining f electrons are kept frozen in the core to treat the localized f electrons for rare earth elements (Pr–Eu and Tb–Lu).[68] The electronic transport calculations were performed using the Boltztrap code[69] with a constant relaxation time of 10^{-14} s. All computations and data analysis were carried out using the Materials Project high-throughput calculation software developed in python: pymatgen,[70] FireWorks,[70,71] and MPWorks (available at www.github.com/materialsproject).

Thermodynamic stability

To assess the thermodynamic stability of a substituted new compound at $T = 0$ K, we compared its energy *versus* the energy of other phases or their linear combinations through the convex hull construction.[46,47] The decomposition energy, E_{decomp} (in eV per atom) of the compound is used to describe its stability *versus* competing phases. Stable compounds have E_{decomp} equal to zero and the larger the decomposition energy, the less stable the material is. However, phases with low to moderate computed E_{decomp} values (*e.g.*, less than 50–100 meV per atom) can be stabilized at some non-zero temperature by entropy or through metastable synthesis methods.

X-ray photoelectron spectroscopy

To verify that f-electrons do not need to be included for accurate transport and defect properties, XPS measurements were compared with HSE06 hybrid DFT calculations for the trigonal bulk structure with f-electrons included as valence. The XPS spectrum of the trigonal phase shows four distinct peaks below the valence band corresponding to Te 5s, Ag 4d, and Tm 4f states (see Fig. S16 in ESI†). The main disagreement between the DFT and XPS results is an upwards shift of the second Tm peak and a downwards shift in the Te peak, which would likely be corrected further with the inclusion of spin–orbit coupling. Overall, the experimental results demonstrate that there is no f-electron character at the VBM, and therefore our choice of pseudopotential and treatment of f-electrons should not influence the calculated transport properties or contribute to the electron chemical potential reference for the defect calculations.

Minimum thermal conductivity

The minimum lattice thermal conductivity (κ_{lat}) was estimated based on the Cahill–Watson–Pohl model,[31] in which the mean-free-path for phonon scattering approaches the inter-atomic spacing, usually described in terms of the longitudinal and transverse sound velocities $v_{\mathrm{L,s}}$ and $v_{\mathrm{T,s}}$, especially in the high temperature limit:[31,72,73]

$$\kappa_{\min} = 0.4 k_{\mathrm{B}} \rho^{2/3} (v_{\mathrm{L,s}} + 2v_{\mathrm{T,s}}), \quad (1)$$

where k_{B} is Planck's constant, ρ is atomic density of the materials. $v_{\mathrm{L,s}}$ and $v_{\mathrm{T,s}}$ can be determined from elastic constants such as bulk modulus (K) and shear modulus (G), predicted from calculations.

$$v_{\mathrm{L,s}} = \left[\frac{K + 4G/3}{\rho}\right]^{\frac{1}{2}} \quad (2)$$

$$v_{\mathrm{T,s}} = (G/\rho)^{1/2}$$

We calculated the 6×6 elastic tensor from first-principles calculations and used Voigt–Reuss–Hill average[74] of bulk and shear modulus in eqn (2). The elastic tensor was fitted from 24 strain–stress pairs of deformed structures generated by applying a small strain on the original structure. Four different magnitudes ($\pm 1\%$ and $\pm 0.5\%$) of the six independent component of Green–Lagrange strain tensor were employed for each structure. The corresponding stress tensor was calculated from DFT calculation for each deformed structure.[75]

Defect thermodynamics

The defect formation energy, which determines the stability of a defect with charge q, is expressed below according to the Zhang–Northrup supercell formalism[76]

$$\Delta H_{\mathrm{d,q}} = \left[E_{\mathrm{d,q}} - E_{\mathrm{b}}\right] + \sum_{\alpha} n_{\alpha}\left(\mu_{\alpha}^{0} + \Delta\mu_{\alpha}\right) + q(E_{\mathrm{VBM}} + V_{\mathrm{PA}} + \mu_{\mathrm{e}}) + \Delta E_{\mathrm{IC}}, \quad (3)$$

where, $E_{\mathrm{d,q}}$ and E_{b} are the total energies of the defect containing supercell and the ideal supercell, respectively. Crystal growth conditions were reflected by the atomic chemical potential, $\mu_{\alpha} = (\mu_{\alpha}^{0} + \Delta\mu_{\alpha})$, where μ_{α}^{0} is the chemical potential of an element in its standard reference state (the phase in equilibrium at 0 K), and $\Delta\mu_{\alpha}$ is the change in chemical potential of an element with reference to its standard state. For a maximally rich growth environment of an element, $\Delta\mu_{\alpha} = 0$. Atoms are either removed ($n_{\alpha} = +1$) or added ($n_{\alpha} = -1$) to the host supercell in the formation of a defect. E_{VBM} is the valence band maximum (VBM) energy and corresponds to the cost of removing an electron from the top of the valence band. It was found that with a change in supercell size (*i.e.*, from $3 \times 3 \times 2$ to $3 \times 3 \times 3$), the defect formation energies only change by <0.05 eV (*i.e.*, ~ 0.02 eV and 0.03 eV for neutral and negatively charged Ag vacancy, respectively), and thus the potential alignment V_{PA} and the image-charge correction energy E_{IC} terms are calculated with the scheme

proposed by Freysoldt, Neugebauer, and Van de Walle (FNV).[77] Defect calculations for $TmAgTe_2$ were performed on a $3 \times 3 \times 2$ supercell that contained 72 atoms (trigonal phase), and on a $3 \times 2 \times 2$ supercell that contained 96 atoms for the $YAgTe_2$ case (tetragonal phase). The calculated dielectric constant of 23.15 is used for the defect formation energy determination within in FNV scheme. Considering that it is more difficult to converge to the ground state of defective systems with f valence electrons compared to bulk systems,[78] we did not study the defect formation energies with f electrons as valence electrons and an onsite Hubbard-type U correction. Moreover, such a neglect of f electron in pseudopotentials of Tm^{3+} might be responsible for the negative defect formation energy for some conditions (as shown in Fig. 4). But the general trend is likely to be captured as we found trigonal $YAgTe_2$ without f electron issues has similar trend for defect formations displaying much less negative values.

Substitution algorithm

We used an ionic substitution algorithm to propose new XYZ_2 materials by substituting ions in $TmAgTe_2$, as available in pymatgen.[19,70] This approach uses information about the substitution probability of ions—obtained by data-mining all known crystalline compounds—to suggest possible substitutions for design of novel compounds.[19]

Sample preparation

A polycrystalline sample of $TmAgTe_2$ was synthesized following a similar route to that previously reported.[27,28] Stoichiometric amounts of elements (Tm = 99.9%; Ag, Te = 99.999%, metals basis, Alfa Aesar) were sealed in a quartz ampoule under vacuum ($\sim 10^{-6}$ mbar). The ampoule was heated in a vertical tube furnace to 1443 K in 30 h and annealed at this temperature for 15 h. The sample was then cooled to 873 K in 30 h and annealed at that temperature for one week followed by quenching in water. Fine powder of the sample was filled into 1/2 inch high-density graphite dies (POCO) under Ar atmosphere and sintered in a hot press[79] at 973 K under 40 MPa pressure for 1 h. To obtain tetragonal $TmAgTe_2$, the hot-pressed sample was sealed in a quartz tube under vacuum and then further annealed at 673 K for 4 d. The pellet showed $>97\%$ of the theoretical density.

Sample characterization

The $TmAgTe_2$ sample was investigated by X-ray diffraction (XRD) using a Philips XPERT MPD diffractometer (Cu-K_α radiation) in reflection mode. Rietveld refinements and the lattice parameter determination (using α-Si as internal standard) were carried out using the WinCSD program package.[80] Energy dispersive X-ray spectroscopy (EDXS) was performed using a Zeiss 1550 VP SEM.

Thermal analysis was carried out using a DSC (Q200 from TA Instruments™). The sample was cycled from 423 K to 773 K at a scanning rate of 10 K min^{-1} under N_2 atmosphere. High temperature transport measurements were carried out up to 673 K and 873 K for the tetragonal and trigonal phases, respectively. The electrical resistivity and Hall coefficient measurements were performed using the van der Pauw technique under a reversible magnetic field of 2 T using pressure-assisted tungsten electrodes.[81] The Seebeck coefficient of the sample was obtained using chromel–Nb thermocouples by applying a temperature gradient across the sample oscillating with ±7.5 K.[82] Thermal diffusivity, D, was measured using the laser flash method (Netzsch LFA 457) under argon atmosphere. Thermal conductivity was calculated by $\kappa = D \times d \times C_p$, where d is the measured density of the material and C_p is the heat capacity at constant pressure. The sample density was measured based on Archimedes' principle. C_p was determined from 273 K to 380 K by relaxation microcalorimetry with a Physical Property Measurement System (PPMS, from Quantum Design) under high vacuum ($<10^{-4}$ Torr) and extrapolated. The relaxation calorimetry technique is described in detail in ref. 53. Diffuse reflectance measurements were performed using a Nicolet 6700 Fourier transform infrared (FTIR) spectrometer with a Praying Mantis (Harrick) attachment.[83] The X-ray photoelectron spectroscopy (XPS) spectrum was generated using a Multilab XPS system with a CLAM4 hemispherical analyzer (Thermo Scientific). A non-monochromatic Mg source was set to 14.5 kV and 20 mA and a pass energy of 20 eV was applied. The electron analyzer was set to a diameter of 600 μm.

Acknowledgements

This work was intellectually led by the Materials Project which is supported by the Department of Energy Basic Energy Sciences program under Grant No. EDCBEE, DOE Contract DE-AC02-05CH11231. This research used resources of the National Energy Research Scientific Computing Center, a DOE Office of Science User Facility supported by the Office of Science of the U.S. Department of Energy. U.A. acknowledges the financial assistance of The Scientific and Technological Research Council of Turkey. J.-H.P. acknowledges the Dalhousie Research in Energy, Advanced Materials and Sustainability (DREAMS) NSERC CREATE program. M.A.W. acknowledges the support of NSERC, and Dalhousie University's Institute for Research in Materials and its Facilities for Materials Characterization. G.H. acknowledges the F.R.S.-FNRS and the European Union Marie Curie Career Integration (CIG) grant HTforTCOs PCIG11-GA-2012-321988 for financial support. Z.M.G. acknowledges the Molecular Materials Research Center (MMRC) at Caltech in the Beckman Institute where optical measurements in this work were performed.

References

1 R. J. Mehta, Y. Zhang, H. Zhu, D. S. Parker, M. Belley, D. J. Singh, R. Ramprasad, T. Borca-Tasciuc and G. Ramanath, *Nano Lett.*, 2012, **12**, 4523–4529.
2 L. D. Zhao, H. J. Wu, S. Q. Hao, C. I. Wu, X. Y. Zhou, K. Biswas, J. Q. He, T. P. Hogan, C. Uher, C. Wolverton, V. P. Dravid and M. G. Kanatzidis, *Energy Environ. Sci.*, 2013, **6**, 3346.
3 X. Shi, J. Yang, J. R. Salvador, M. Chi, J. Y. Cho, H. Wang, S. Bai, J. Yang, W. Zhang and L. Chen, *J. Am. Chem. Soc.*, 2011, **133**, 7837–7846.

4 J. Yang, H. Li, T. Wu, W. Zhang, L. Chen and J. Yang, *Adv. Funct. Mater.*, 2008, **18**, 2880–2888.
5 W. G. Zeier, H. Zhu, Z. M. Gibbs, G. Ceder, W. Tremel and G. J. Snyder, *J. Mater. Chem. C*, 2014, **2**, 10189–10194.
6 G. Hautier, A. Jain and S. P. Ong, *J. Mater. Sci.*, 2012, **47**, 7317–7340.
7 S. Curtarolo, G. L. W. Hart, M. B. Nardelli, N. Mingo, S. Sanvito and O. Levy, *Nat. Mater.*, 2013, **12**, 191–201.
8 L. Vitos, P. A. Korzhavyi and B. Johansson, *Nat. Mater.*, 2003, **2**, 25–28.
9 G. Ceder, *Mater. Res. Soc. Bull.*, 2010, **35**, 693–702.
10 L.-C. Lin, A. H. Berger, R. L. Martin, J. Kim, J. A. Swisher, K. Jariwala, C. H. Rycroft, A. S. Bhown, M. W. Deem, M. Haranczyk and B. Smit, *Nat. Mater.*, 2012, **11**, 633–641.
11 J. Greeley, T. F. Jaramillo, J. Bonde, I. B. Chorkendorff and J. K. Nørskov, *Nat. Mater.*, 2006, **5**, 909–913.
12 J. Carrete, N. Mingo, S. Wang and S. Curtarolo, *Adv. Funct. Mater.*, 2014, **24**, 7427.
13 I. Opahle, A. Parma, E. J. McEniry, R. Drautz and G. K. H. Madsen, *New J. Phys.*, 2013, **15**, 105010.
14 L. Bjerg, G. K. H. Madsen and B. B. Iversen, *Chem. Mater.*, 2011, **23**, 3907–3914.
15 G. K. H. Madsen, *J. Am. Chem. Soc.*, 2006, **128**, 12140–12146.
16 S. Wang, Z. Wang, W. Setyawan, N. Mingo and S. Curtarolo, *Phys. Rev. X*, 2011, **1**, 1–8.
17 H. Zhu, W. Sun, R. Armiento, P. Lazic and G. Ceder, *Appl. Phys. Lett.*, 2014, **104**, 082107.
18 G. Hautier, A. Miglio, G. Ceder, G.-M. Rignanese and X. Gonze, *Nat. Commun.*, 2013, **4**, 2292.
19 G. Hautier, C. Fischer, V. Ehrlacher, A. Jain and G. Ceder, *Inorg. Chem.*, 2011, **50**, 656–663.
20 G. Bergerhoff and I. D. Brown, *Crystallographic Databases*, International Union of Crystallography, Chester, 1987.
21 A. Belsky, M. Hellenbrandt, V. L. Karen and P. Luksch, *Acta Crystallogr., Sect. B: Struct. Sci.*, 2002, **58**, 364–369.
22 J. Zhang, R. Liu, N. Cheng, Y. Zhang, J. Yang, C. Uher, X. Shi, L. Chen and W. Zhang, *Adv. Mater.*, 2014, **26**, 3848–3853.
23 C. Delmas, C. Fouassier and P. Hagenmuller, *Physica B+C*, 1980, **99**, 81–85.
24 R. Liu, L. Xi, H. Liu, X. Shi, W. Zhang and L. Chen, *Chem. Commun.*, 2012, **48**, 3818–3820.
25 H. Lin, H. Chen, J.-N. Shen, L. Chen and L.-M. Wu, *Chem. – Eur. J.*, 2014, **20**, 15401–15408.
26 M.-P. Pardo, M. Julien-Pouzol and J. Flahaut, *C. R. Acad. Sci. C*, 1973, **276**, 599.
27 L. D. Gulay, I. D. Olekseyuk and A. Pietraszko, *J. Alloys Compd.*, 2006, **424**, 159–163.
28 L. D. Gulay, J. Stpień-Damm, M. Daszkiewicz and A. Pietraszko, *J. Alloys Compd.*, 2007, **431**, L1–L3.
29 B. Eisenmann and H. Schafer, *Landolt–Bornstein: Group III condensed matter: numerical data and functional relationships in science and technology*, Springer-Verlag, 1986, vol. 14b1: sulf.
30 D. P. Spitzer, *J. Phys. Chem. Solids*, 1970, **31**, 19.
31 D. Cahill, S. Watson and R. Pohl, *Phys. Rev. B: Condens. Matter Mater. Phys.*, 1992, **46**, 6131–6140.
32 L. Vočadlo, J. Poirer and G. Price, *Am. Mineral.*, 2000, **85**, 1–6.
33 F. Murnaghan, *Proc. Natl. Acad. Sci. U. S. A.*, 1944, **30**, 244.
34 E. S. Toberer, A. Zevalkink and G. J. Snyder, *J. Mater. Chem.*, 2011, **21**, 15843.
35 G. A. Slack, *Solid State Phys.*, 1979, **34**, 1–73.
36 Y. Pei, N. A. Heinz and G. J. Snyder, *J. Mater. Chem.*, 2011, **21**, 18256.
37 B. Du, H. Li, J. Xu, X. Tang and C. Uher, *Chem. Mater.*, 2010, **22**, 5521–5527.
38 T. Plirdpring, K. Kurosaki, A. Kosuga, T. Day, S. Firdosy, V. Ravi, G. J. Snyder, A. Harnwunggmoung, T. Sugahara, Y. Ohishi, H. Muta and S. Yamanaka, *Adv. Mater.*, 2012, **24**, 3622362.
39 H. Liu, X. Shi, F. Xu, L. Zhang, W. Zhang, L. Chen, Q. Li, C. Uher, T. Day and G. J. Snyder, *Nat. Mater.*, 2012, **11**, 422425.
40 P. Qiu, T. Zhang, Y. Qiu, X. Shi and L. Chen, *Energy Environ. Sci.*, 2014, **7**, 4000–4006.
41 M. Oudah, K. M. Kleinke and H. Kleinke, *Inorg. Chem.*, 2015, **54**, 845.
42 Y. Pei, H. Wang and G. J. Snyder, *Adv. Mater.*, 2012, **24**, 6125–6135.
43 H. J. Goldsmid, *J. Electron. Mater.*, 2012, **42**, 1482–1489.
44 J. Yan, P. Gorai, B. Ortiz, S. Miller, S. A. Barnett, T. Mason, V. Stevanović and E. S. Toberer, *Energy Environ. Sci.*, 2014, **8**, 983–994.
45 Y. Pei, X. Shi, A. LaLonde, H. Wang, L. Chen and G. J. Snyder, *Nature*, 2011, **473**, 66–69.
46 S. P. Ong, L. Wang, B. Kang and G. Ceder, *Chem. Mater.*, 2008, **20**, 1798–1807.
47 S. P. Ong, A. Jain, G. Hautier, B. Kang and G. Ceder, *Electrochem. Commun.*, 2010, **12**, 427.
48 C. Bera, S. Jacob, I. Opahle, N. S. H. Gunda, R. Chmielowski, G. Dennler and G. K. H. Madsen, *Phys. Chem. Chem. Phys.*, 2014, **16**, 19894.
49 L. Yang and G. Ceder, *Phys. Rev. B: Condens. Matter Mater. Phys.*, 2013, **88**, 224107.
50 J. C. Slater, *J. Chem. Phys.*, 1964, **41**, 3199.
51 G. Tan, L.-D. Zhao, F. Shi, J. W. Doak, S.-H. Lo, H. Sun, C. Wolverton, V. P. Dravid, C. Uher and M. G. Kanatzidis, *J. Am. Chem. Soc.*, 2014, **136**, 7006–7017.
52 H. Wang, Z. M. Gibbs, Y. Takagiwa and G. J. Snyder, *Energy Environ. Sci.*, 2014, **7**, 804.
53 T. Day, F. Drymiotis, T. Zhang, D. Rhodes, X. Shi, L. Chen and G. J. Snyder, *J. Mater. Chem. C*, 2013, **1**, 7568.
54 C. A. Kennedy, M. Stancescu, R. A. Marriott and M. A. White, *Cryogenics*, 2007, **47**, 107.
55 S. Novikova and N. Abrikosov, *Phys. Solid State*, 1964, **5**, 1397.
56 Z. M. Gibbs, H. Kim, H. Wang, R. L. White, F. Drymiotis, M. Kaviany and G. Jeffrey Snyder, *Appl. Phys. Lett.*, 2013, **103**, 262109.
57 M. Ferhat and J. Nagao, *J. Appl. Phys.*, 2000, **88**, 813.
58 L. Crismat and B. Mar, *Chem. Mater.*, 2011, **23**, 2510–2513.
59 Y. He, T. Day, T. Zhang, H. Liu, X. Shi, L. Chen and G. J. Snyder, *Adv. Mater.*, 2014, **26**, 3974–3978.
60 G. Kresse and J. Furthmuller, *Phys. Rev. B: Condens. Matter Mater. Phys.*, 1996, **54**, 11169.

61 J. P. Perdew, K. Burke and M. Ernzerhof, *Phys. Rev. Lett.*, 1996, **77**, 3865.
62 J. P. Perdew, K. Burke and M. Ernzerhof, *Phys. Rev. Lett.*, 1997, **78**, 1396.
63 P. E. Blochl, *Phys. Rev. B: Condens. Matter Mater. Phys.*, 1994, **50**, 17953.
64 B. Meredig, A. Thompson, H. A. Hansen, C. Wolverton and A. van de Walle, *Phys. Rev. B: Condens. Matter Mater. Phys.*, 2010, **82**, 195128.
65 F. Zhou and V. Ozoliš, *Phys. Rev. B: Condens. Matter Mater. Phys.*, 2009, **80**, 125127.
66 J. P. Allen and G. W. Watson, *Phys. Chem. Chem. Phys.*, 2014, **16**, 21016.
67 E. Rogers, P. Dorenbos and E. van der Kolk, *New J. Phys.*, 2011, **13**, 093038.
68 http://cms.mpi.univie.ac.at/vasp/vasp/vasp.html.
69 G. K. H. Madsen and D. J. Singh, *Comput. Phys. Commun.*, 2006, **175**, 67–71.
70 S. P. Ong, W. D. Richards, A. Jain, G. Hautier, M. Kocher, S. Cholia, D. Gunter, V. L. Chevrier, K. A. Persson and G. Ceder, *Comput. Mater. Sci.*, 2013, **68**, 314–319.
71 A. Jain, S. P. Ong, W. Chen, B. Medasani, X. Qu, M. Kocher, M. Brafman, G. Petretto, G.-M. Rignanese, G. Hautier, D. Gunter and K. A. Persson, *Concurrency and Computation: Practice and Experience*, 2015, DOI: 10.1002/cpe.3505.
72 D. G. Cahill, P. V. Braun, G. Chen, D. R. Clarke, S. Fan, K. E. Goodson, P. Keblinski, W. P. King, G. D. Mahan, A. Majumdar, H. J. Maris, S. R. Phillpot, E. Pop and L. Shi, *Appl. Phys. Rev.*, 2014, **1**, 011305.
73 S. Lee, K. Esfarjani, T. Luo, J. Zhou, Z. Tian and G. Chen, *Nat. Commun.*, 2014, **5**, 3525.
74 R. Hill, *Proc. Phys. Soc. A*, 1952, **65**, 349.
75 M. de Jong, W. Chen, T. Angsten, A. Jain, R. Notestine, A. Gamst, M. Sluiter, C. Krishna Ande, S. van der Zwaag, J. J. Plata, C. Toher, S. Curtarolo, G. Ceder, K. A. Persson and M. Asta, *Sci. Data*, 2015, DOI: 10.1038/sdata.2015.9.
76 S. B. Zhang and J. E. Northrup, *Phys. Rev. Lett.*, 1991, **67**, 2339–2342.
77 C. Freysoldt, J. Neugebauer and C. Van de Walle, *Phys. Rev. Lett.*, 2009, **102**, 016402.
78 B. Dorado, M. Freyss, B. Amadon, M. Bertolus, G. Jomard and P. Garcia, *J. Phys.: Condens. Matter*, 2013, **25**, 333201.
79 A. D. LaLonde, T. Ikeda and G. J. Snyder, *Rev. Sci. Instrum.*, 2011, **82**, 025104.
80 L. Akselrud and Y. Grin, *J. Appl. Crystallogr.*, 2014, **47**, 803–805.
81 K. A. Borup, E. S. Toberer, L. D. Zoltan, G. Nakatsukasa, M. Errico, J.-P. Fleurial, B. B. Iversen and G. J. Snyder, *Rev. Sci. Instrum.*, 2012, **83**, 123902.
82 S. Iwanaga, E. S. Toberer, A. LaLonde and G. J. Snyder, *Rev. Sci. Instrum.*, 2011, **82**, 063905.
83 Z. M. Gibbs, A. LaLonde and G. J. Snyder, *New J. Phys.*, 2013, **15**, 075020.
84 K. Biswas, J. He, I. D. Blum, C.-I. Wu, T. P. Hogan, D. N. Seidman, V. P. Dravid and M. G. Kanatzidis, *Nature*, 2012, **489**, 414–418.
85 H. Wang, Y. Pei, A. D. Lalonde and G. J. Snyder, *Adv. Mater.*, 2011, **23**, 1366.
86 D. T. Morelli, T. Caillat, J.-P. Fleurial, A. Borshchevsky, J. Vandersande, B. Chen and C. Uher, *Phys. Rev. B: Condens. Matter Mater. Phys.*, 1995, **51**, 9622.
87 M. S. Toprak, C. Stiewe, D. Platzek, S. Williams, L. Bertini, E. Muller, C. Gatti, Y. Zhang, M. Rowe and M. Muhammed, *Adv. Funct. Mater.*, 2004, **14**, 1189–1196.
88 G. A. Slack and M. A. Hussain, *J. Appl. Phys.*, 1991, **70**, 2694.
89 X. W. Wang, H. Lee, Y. C. Lan, G. H. Zhu, G. Joshi, D. Z. Wang, J. Yang, A. J. Muto, M. Y. Tang, J. Klatsky, S. Song, M. S. Dresselhaus, G. Chen and Z. F. Ren, *Appl. Phys. Lett.*, 2008, **93**, 193121.
90 Y. Xia, V. Ponnambalam, S. Bhattacharya, A. L. Pope, S. J. Poon and T. M. Tritt, *J. Phys.: Condens. Matter*, 2001, **13**, 77.
91 T. Borca-Tasciuc, D. Achimov, W. L. Liu, G. Chen, H.-W. Ren, C.-H. Lin and S. S. Pei, *Microscale Thermophys. Eng.*, 2001, **5**, 225.
92 W. U. J. Roland, *Semicond. Semimetals*, 1972, **8**, 67–102.
93 S. Adachi, *J. Appl. Phys.*, 2007, **102**, 063502.
94 A. M. Dehkordi, S. Bhattacharya, T. Darroudi, J. W. Gra, U. Schwingenschlo, H. N. Alshareef and T. M. Tritt, *Chem. Mater.*, 2014, **26**, 2478–2485.
95 K. Koumoto, Y. Wang, R. Zhang, A. Kosuga and R. Funahashi, *Annu. Rev. Mater. Res.*, 2010, **40**, 363–394.